Monthly Notices
of the
ROYAL ASTRONOMICAL SOCIETY

MNRAS **487,** 3679–3692 (2019)
Advance Access publication 2019 June 6

doi:10.1093/mnras/stz1572

A nuclear ionized gas outflow in the Seyfert 2 galaxy UGC 2024

Dania Muñoz-Vergara,[1,2★] Neil M. Nagar,[1★] Venkatessh Ramakrishnan,[1] Carolina Finlez,[1] Thaisa Storchi-Bergmann,[3] Roy Slater,[4] Veronica Firpo,[2,5] Pedro K. Humire,[1] Pamela Soto-Pinto,[1] Steven B. Kraemer,[6] Davide Lena,[7,8] Andrew Robinson,[9] Rogemar A. Riffel,[10] D. Michael Crenshaw,[11] Martin S. Elvis,[12] T. C. Fischer,[13] Allan Schnorr-Müller[3] and Henrique R. Schmitt[14]

[1]*Departamento de Astronomía, Universidad de Concepción, Concepción, Chile*
[2]*Departamento de Física y Astronomía, Universidad de La Serena, La Serena, Chile*
[3]*Instituto de Física, CP 15015, Universidade Federal do Rio Grande do Sul, 91501-970, Porto Alegre, RS, Brazil*
[4]*Dirección de Formación General, Facultad de Educación y Cs. Sociales, Universidad Andres Bello, Sede Concepción, autopista Concepción-Talcahuano 7100, Talcahuano, Chile*
[5]*Gemini Observatory, Southern Operations centre, La Serena, Chile*
[6]*Institute for Astrophysics and Computational Sciences, Department of Physics, The Catholic University of America, Washington, DC 20064, USA*
[7]*SRON, Netherlands Institute for Space Research, Sorbonnelaan 2, NL-3584 CA Utrecht, the Netherlands*
[8]*Department of Astrophysics/IMAPP, Radboud University, Nijmegen, PO Box 9010, NL-6500 GL Nijmegen, the Netherlands*
[9]*Department of Physics, Rochester Institute of Technology, 84 Lomb Memorial Drive, Rochester, NY 14623, USA*
[10]*Universidade Federal de Santa Maria, Departamento de Física, Centro de Ciências Naturais e Exatas, 97105-900, Santa Maria, RS, Brazil*
[11]*Department of Physics and Astronomy, Georgia State University, Astronomy Offices, 25 Park Place, Suite 605, Atlanta, GA 30303, USA*
[12]*Harvard-Smithsonian Center for Astrophysics 60 Garden St., ms.6, Cambridge, MA 02138 USA*
[13]*Astrophysics Science Division, Goddard Space Flight Center, Code 665, Greenbelt, MD 20771, USA*
[14]*Naval Research Laboratory, Washington, DC 20375, USA*

Accepted 2019 May 30. Received 2019 May 27; in original form 2018 January 18

ABSTRACT

As part of a high-resolution observational study of feeding and feedback processes occurring in the vicinity of the active galactic nucleus in 40 galaxies, we observed the inner 3.″5 × 5 arcsec of the nearby spiral and Seyfert 2 galaxy UGC 2024 with the integral field unit of the Gemini-South Telescope. The observations enabled a study of the stellar and gas kinematics in this region at a spatial resolution of 0.″5 (218 pc), and a spectral resolution of 36 km s^{-1} over the wavelength range 4100–7300 Å. For the strongest emission-lines (H β, [O III] λ5007 Å, H α, [N II] λ6584 Å, and [S II] λλ6717,6731 Å) we derived maps of the flux, radial velocity, and velocity dispersion. The flux distribution and kinematics of the [O III] emission line are roughly symmetric around the nucleus: the radial velocity is close to systemic over the full field of view. The kinematics of the other strong emission lines trace both this systemic velocity component, and ordered rotation (with kinematic centre 0.″2 north-west of the nucleus). The stellar continuum morphology and kinematics are, however, asymmetrical around the nucleus. We interpret these unusual kinematics as the superposition of a component of gas rotating in the galaxy disc plus a 'halo' component of highly ionized gas. This halo either traces a quasi-spherical fountain with average radial velocity 200 km s^{-1}, in which case the total nuclear outflow mass and momentum are 2 × 10^5 M$_\odot$ and 4 × 10^7 M$_\odot$ km s^{-1}, respectively, or a dispersion supported halo created by a past nuclear starburst.

Key words: galaxies: active – galaxies: individual: UGC 2024 – galaxies: kinematics and dynamics – galaxies: nuclei – galaxies: Seyfert.

1 INTRODUCTION

Understanding how mass is transferred from galactic scales down to nuclear scales to feed the supermassive black hole (hereafter SMBH) has been a long-standing problem, given that it is widely accepted that the prodigious energy emitted by the active galactic

★ E-mail: daniamunozv@gmail.com (DMV); nagar@astro-udec.cl (NMN)

nucleus (AGN) is the result of accretion onto the SMBH (Lynden-Bell 1969; Soltan 1982).

Theoretical studies and simulations (Shlosman, Begelman & Frank 1990; Emsellem, Goudfrooij & Ferruit 2003; Knapen 2005; Emsellem et al. 2006) have shown that non-axisymmetric potentials efficiently promote gas inflow towards the inner regions. Structures such as nuclear bars (Englmaier & Shlosman 2004), spiral arms, and small-scale discs are commonly observed in the inner kpc of galaxies with an AGN (Davies 1972; Ellison et al. 2013; Schnorr-Müller et al. 2014b; Lena et al. 2015; Schnorr-Müller et al. 2017a,b), with mass inflow rates of gas on kpc to 100 pc scales ranging from 10^{-3} to 10^{-1} $M_{\odot}$ yr^{-1} (e.g. Riffel 2013).

While the mechanisms that trigger inflows of cold gas are difficult to identify, the feedback produced by an AGN, usually traced by outflows, is easier to observe (Riffel 2013). These have been observed in ionized gas emission from the Narrow Line Region (NLR) where the emission lines typically have widths of 500 km s^{-1}. Mass outflow rates in ionized gas are 10–1000 times larger than the AGN mass accretion rates (Crenshaw, Kraemer & George 2003; Veilleux, Cecil & Bland-Hawthorn 2005; Crenshaw & Kraemer 2012; Riffel 2013; Revalski et al. 2018), supporting an origin for the bulk of the outflow as gas from the galaxy plane entrained by a nuclear jet or accretion disc wind (Storchi-Bergmann 2010).

Numerous studies of prominent optical emission lines have revealed that the NLR is an ideal place to witness AGN feedback in the form of ionized gas outflows (Storchi-Bergmann 2010; Riffel & Storchi-Bergmann 2011; Bergmann 2012; Bae & Woo 2016, and references therein). The excitation and dynamics of the inner NLR gas can reveal how radiation and mass outflows from the nucleus interact with the circumnuclear gas. Crenshaw & Kraemer (2000b) constructed a simple 3D model of a biconical outflow to reproduce the observed position–velocity (PV) diagrams of the Seyfert galaxy NGC 1068 obtained from *Hubble Space Telescope* (*HST*) STIS long-slit data. Since then, biconical outflows associated with ionized gas have been reported and modelled by many authors, (e.g. Crenshaw & Kraemer 2000a; Veilleux, Shopbell & Miller 2001; Fischer et al. 2010; Storchi-Bergmann 2010; Fischer et al. 2013; Barbosa et al. 2014; Lena et al. 2015; Humire et al. 2018).

Here, we present an analysis of the stellar and gas kinematics in the inner kpc of UGC 2024, as derived from integral field unit (IFU) observations carried out with the Gemini South telescope. UGC 2024, earlier classified as an Sab galaxy (Huchra, Vogeley & Geller 1999) is more likely an SBab galaxy with a bar of 8.95 kpc (Paturel et al. 2003; Nair & Abraham 2010), and harbors a Seyfert 2 nucleus (Toba et al. 2013). It shows weak broad permitted lines in the near-IR implying that the broad lines may be dust obscured in the optical (Heisler & De Robertis 1999). UGC 2024 is at a luminosity distance of 90 Mpc (Crook et al. 2007), which corresponds to an angular scale of 0.436 kpc $arcsec^{-1}$ (assuming $H_0 = 73$ km s^{-1} Mpc^{-1}, $\Omega_{matter} = 0.027$ and $\Omega_{vacuum} = 0.73$). A major axis position angle (from north to east; hereafter PA) of 150° was derived by Schmitt & Kinney (2000) via ellipse fitting to ground-based *I*-band images. The inclination of the galaxy is 48°,[1] computed from the apparent axial ratio listed in the UGC catalogue. Giuricin, Mezzetti & Mardirossian (1985) determined the linear diameter at the 25 B-mag $arcsec^{-2}$ brightness level and the total blue luminosity, obtaining $D \approx 22.38$ kpc and $L_B \approx 2.08 \times 10^{10}$ $L_{\odot}$. The latest heliocentric radial velocity published for this galaxy is 6699 km s^{-1}, i.e. a redshift of $z \sim 0.022347 \pm 0.000010$.[2]

Gelbord, Mullaney & Ward (2009) found that both the high-ionization ([Fe VII], [Fe X] λ6374 Å, [Fe XI] λ 7892 Å), medium-ionization ([O III] λ5007 Å), and low-ionization forbidden lines ([O I] λλ6300,6363 Å, [N II] λλ6548,6584 Å and [S II] λλ6717,6731 Å) in UGC 2024 are less redshifted than the host galaxy. That is, the velocities measured by fitting Gaussian to each line are lower than the host galaxy systemic velocity as derived from the [S II] λλ6717,6731 Å emission-lines. They interpret this difference as due to (blueshifted) outflow velocities along our line of sight, but did not rule out the possibility of emission from infalling clouds on the far side of the AGN.

UGC 2024 has an unresolved nuclear radio source (Kinney et al. 2000; Schmitt & Kinney 2000) with a size < 45 pc (Schmitt et al. 2001). Earlier studies of the optical continuum and the H α emission-line (Heisler & Vader 1994, 1995) show that UGC 2024 presents a faint halo surrounding its nucleus. This galaxy also shows two small spiral arms which extend into its faint outer halo; 'unsharp masked' and (*B* – *R*) colour images reveal many bright knots (H II regions) at either side of the nucleus along the same line as the spiral arms (Heisler & Vader 1994) even through the spiral arms are not strong H α emitters. Heisler & Vader (1995) conclude that UGC 2024 is either an early-type spiral or that the arms are tidal tails of older stars pulled out during a previous interaction.

Schmitt et al. (2003) found that UGC 2024 shows extended diffuse [O III] emission, with no clear conical shape. This emission is extended by 1.″45 × 2.″6 (minor axis × major axis extension) with the major axis along PA = 145°, within 5° from the host galaxy major axis (Schmitt et al. 2003). Goto (2006) compared the spatial flux distributions of the [O III] emission line with the H δ absorption line in order to study the post-starburst (PS) region in UGC 2024. They stressed that, even if both lines 'peak' at the centre, H δ is more extended (with extension greater than ±2 arcsec). On the other hand, the [O III] equivalent width (EW) is larger than the H δ EW (6–12 Å and 3–5 Å, respectively) within the central ±2 arcsec, and for [O III] this value decreases outside this radius, while the H δ EW stays almost constant until ±4 arcsec. Furthermore, they found that the [S II]/H α flux ratio peaks at the nucleus. Based on all these factors, they conclude that the AGN and PS regions are both centrally concentrated, but that the PS region is more extended than the emission-line region.

It is now generally accepted that PS galaxy samples would be only 50 per cent complete if we do not consider narrow-line AGNs (Wild et al. 2007; Sell et al. 2014; Pawlik et al. 2018), and that PS are in a transition phase between the blue cloud and the red sequence (Pawlik et al. 2018). However, there has been a standing controversy over whether the starburst phase occurs before the inflows that fuel the AGN or whether the AGN ignition fuels the posterior starburst activity (Goto 2006). Given that the line ratios and kinematics in the nucleus of UGC 2024 reflects both its AGN and PS nature, it is a good target in which to improve our understanding of the relationship between PS and AGNs.

The results presented here on UGC 2024 are part of a larger study of a sub-sample of 40 galaxies with extended NLR from the work of Schmitt et al. (2003), with both optical IFU (e.g. Schnorr-Müller et al. 2014b; Lena et al. 2015; Schnorr-Müller et al. 2017a,b; Humire et al. 2018) and ALMA (e.g. Finlez et al. 2018;

[1] https://ned.ipac.caltech.edu

[2] Sloan Digital Sky Survey Data Release 13 as obtained 2017 January 31, from http://www.sdss.org/dr13/data_access/bulk/

Slater et al. 2018) with the aim of study feeding and feedback processes occurring in the vicinity of the AGN. While the results on each galaxy are often sufficiently complex to warrant their own publication, on completion of the sample we will address the larger science goals with this statistically meaningful sample. This paper is organized as follows. In Section 2, we present the observations and data processing. Our results are presented in Section 3. In Section 4, we discuss our results and in Section 5 we present the main conclusions of the paper.

2 OBSERVATION AND DATA REDUCTION

UGC 2024 was observed on 2014 December 1 with the IFU (Allington-Smith et al. 2002) of the Gemini Multi-Object Spectrograph[3] (Hook et al. 2004, with the new Hamamatsu detector array) mounted on the Gemini South Telescope (program ID: GS-2014B-Q-20, PI Nagar). We observed this galaxy in the one-slit mode, covering a Field of View (FOV) of $3\farcs5 \times 5$ arcsec, with a sampling of $0\farcs2$, centred on the nucleus of UGC 2024. The four exposures, each of 900 s, were slightly shifted in position (two positions offset by $0\farcs5$) and central wavelength (two wavelength settings offset by 50 Å), so that the posterior cube combination would correct for detector defects and chip gaps. The seeing during our science observations was estimated using the average full width at half-maximum (FWHM) of three stars in the science acquisition image; we obtain a value of $0\farcs48$, corresponding to 0.218 kpc at the distance of UGC 2024. The longer axis of the IFU was aligned to $\mathrm{PA_{obs}} = 142^{\circ}$, close to the major axis of the host galaxy (major axis PA $\approx 150^{\circ}$). Thus, in the images shown in this work, the major axis of the galaxy appears along $\mathrm{PA_{img}} = 8^{\circ}$ (counterclockwise from the y-axis).

No flux standard star was observed on the same night as the science observations. The UGC 2024 data were thus flux calibrated using an observation of the standard star LTT 2415,[4] which was observed as part of the same program on 2014 October 11 (i.e. more than a month earlier) with the same instrument set-up and an exposure time of 600 s, and under similar observing conditions. We also tested our absolute flux calibration with that of the SDSS (3 arcsec fibre) spectrum, and found overall consistent results. Given the above, while the relative flux calibration of the data is good, we estimate that the absolute calibration has a 30 per cent error.

Data processing was performed with the Gemini IRAF[5] package provided by the Gemini Observatory and specifically developed for the GMOS[6] instrument, following the procedure outlined in Lena (2014). This standard data processing included bias subtraction, overscan, flat-fielding, wavelength calibration, differential atmospheric refraction correction (using the GCUBE task in the GMOS package of IRAF) and building of the data cubes at a spatial sampling of 0.08×0.08 arcsec^2 pixel^{-1}. The final cube contains 2928 spectra over a field of $3\farcs84 \times 4\farcs88$ (48×61 fibres^2).

We used the B600 grating set to a central wavelength of 5700 Å or 5750 Å. The resulting wavelength coverage, 4200 − 7300 Å, covers the H β, [O III] λλ4959,5007 Å, H α, [N II] λλ6548,6584 Å and [S II] λλ6717,6731 Å emission lines, with a spectral resolution as measured from the wavelength calibrated arc spectra, of FWHM = 36 km s^{-1}, i.e. R = 3534 at 6440 Å. Unfortunately, in two of the exposures, the [O III] λ5007 Å emission line fell partially on a CCD chip gap. For these two exposures, we masked 64 Å of data centred on 5119 Å (the central observed wavelength of the [O III] line) before combining the cubes.

The spectrum near the [S II] doublet is affected by the atmospheric Telluric lines. We roughly corrected for this using the standard star spectrum, noting that this star was observed on a different night from the science target. We first fit a black body to the V, R, I, J, H, and K-band magnitudes of the standard star, and then divided the integrated spectrum of the standard star by the black body to recover the effect of telluric absorption on the standard star. This was used to correct the spectra of UGC 2024 near the [S II] emission doublet, taking into account the airmass difference between the galaxy and standard star observations. The telluric subtraction is not optimal, but it only affects less than the 50 per cent of the [S II] λ6717 Å emission line and few of our results depend on this.

3 RESULTS

Fig. 1 illustrates our Gemini/GMOS-IFU observations. The upper left panel shows the acquisition image of UGC 2024, and the upper right panel shows a large-scale UGC 2024 *unsharp*[7] image obtained from the Wide Field Planetary Camera 2 (WFPC2) through the F547M filter aboard the *HST*.[8] In both the acquisition image and large-scale image, the rectangles delimit the FOV of our Gemini GMOS/IFU observations. In the lower panels, we show spectra of the apertures marked in black in the large-scale image. Aperture 1 is the nuclear spectrum (defined by the peak of the stellar continuum). It shows narrow (average central velocity dispersion of 78 km s^{-1}) emission-lines and a [N II]/H α ratio of 1. The spectrum shown here has not yet been corrected for Telluric absorption (see previous section) and thus absorption lines are seen near the [S II] doublet.

The large-scale image in Fig. 1 shows some evidence of dust towards the SW: highlighted by irregular contours and confirmed by the extension of the light distribution in the acquisition image and the continuum (see Figs 1 and 7, respectively). The arms are aligned roughly along the major axis of the galaxy so that the south arm has redshifted velocities and the north arm has blueshifted ones (see Figs 2 and 3). The morphology and kinematics of the spiral arms (under the assumption of trailing spiral arms; Binney & Tremaine 2008), and the dust structures, lead us to infer that the SW side of the galaxy disc is the near side. This interpretation of the near and far sides of the galaxy disc is supported by the H α/H β ratio across the disc (for a wider discussion see Section 3.5).

3.1 Stellar kinematics

To determine the stellar kinematics, we used the Penalized Pixel-Fitting (PPXF) code (Cappellari & Emsellem 2004; Cappellari 2017)

[3]For more details visit:http://www.gemini.edu/sciops/instruments/gmos-0.
[4]Standard Star Atlas for Kyoto3DII, Kyoto3DII Team (2007).
[5]IRAF is the Image Reduction and Analysis Facility, a general purpose software system for the reduction and analysis of astronomical data. IRAF is written and supported by the National Optical Astronomy Observatories (NOAO) in Tucson, Arizona. NOAO is operated by the Association of Universities for Research in Astronomy (AURA), Inc. under cooperative agreement with the National Science Foundation.
[6]http://www.gemini.edu/sciops/data-and-results/processing-software?q=node/11822
[7]Obtained using the unsharp_mask.pro IDL routine for math-image processing. For more details visit https://www.harrisgeospatial.com/docs/unsharp_mask.html.
[8]Obtained from the Hubble Legacy Archive (http://hla.stsci.edu/hlaview.html).

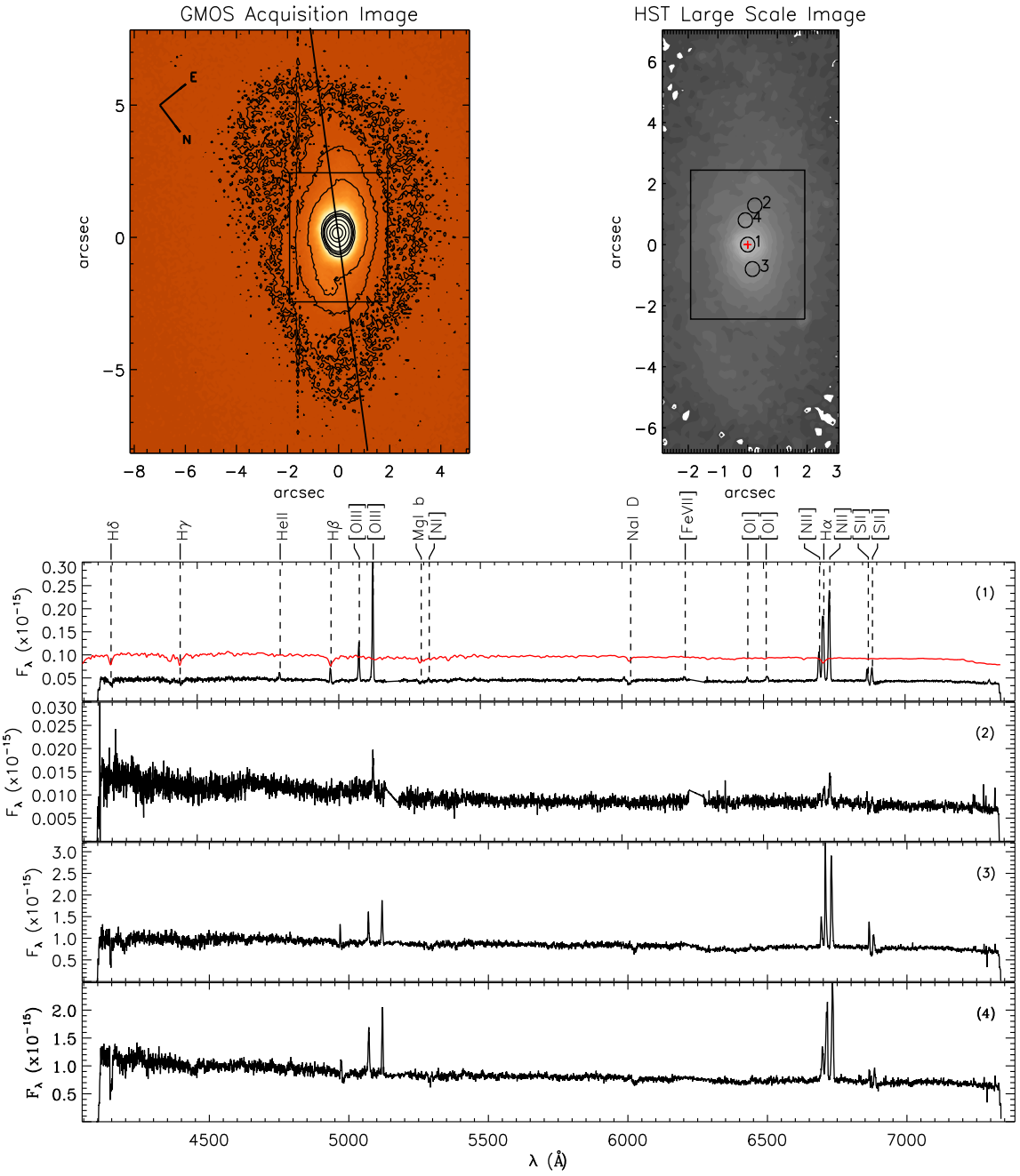

Figure 1. Top left: Gemini/GMOS acquisition image. Black contours are plotted in order to better visualize the spiral arm pattern and the nuclear peak. Top right: a large-scale UGC 2024 image obtained from a *HST* F547M image (see the text); the (red) cross marks the nucleus (the continuum peak). The black and white rectangles delimit the FOV of the GMOS-IFU observations in the acquisition image and large-scale image, respectively. The N-E orientation is indicated by the compass shown in the acquisition image and the solid black line shows the major axis PA; both images have the same orientation. Bottom: spectra (in erg s^{-1} cm^{-2} Å^{-1}) of each of the four marked points in the *HST* large-scale image are shown in black lines. The red spectrum of Aperture 1 shows the best-fitting stellar template to the observed spectrum, as obtained by PPXF (see the text), scaled up for better visualization. Spectra 3 and 4 were extracted from the combined cube, while Spectra 1 and 2 were extracted from the two exposures which fully covered the [O III] line (see the text).

together with a subset of the MILES Library of Stellar Spectra (Sánchez-Blázquez et al. 2006). The 985 template spectra cover the wavelength range 3525–5700 Å at a spectral resolution of 2.51 Å (Falcón-Barroso et al. 2011, $\sigma \sim 64$ km s^{-1}). Before running PPXF, we binned the spaxels of the cube using VORONOI_2D_BINNING[9] (Cappellari & Copin 2003) obtaining 822 bins with a minimum signal-to-noise (S/N) ratio of 25 in the continuum close to the [O III] line. The error spectrum input to PPXF was based on the rms (and thus S/N) calculated over the range 5700–5800 Å for each spectrum, and assuming that this rms reflected the noise over the full spectral range. Fig. 1 shows the best-fitting template spectrum for the nuclear aperture obtained by PPXF (red; for better visualization this template has been scaled up by factor 2).

[9] https://www-astro.physics.ox.ac.uk/~mxc/software/

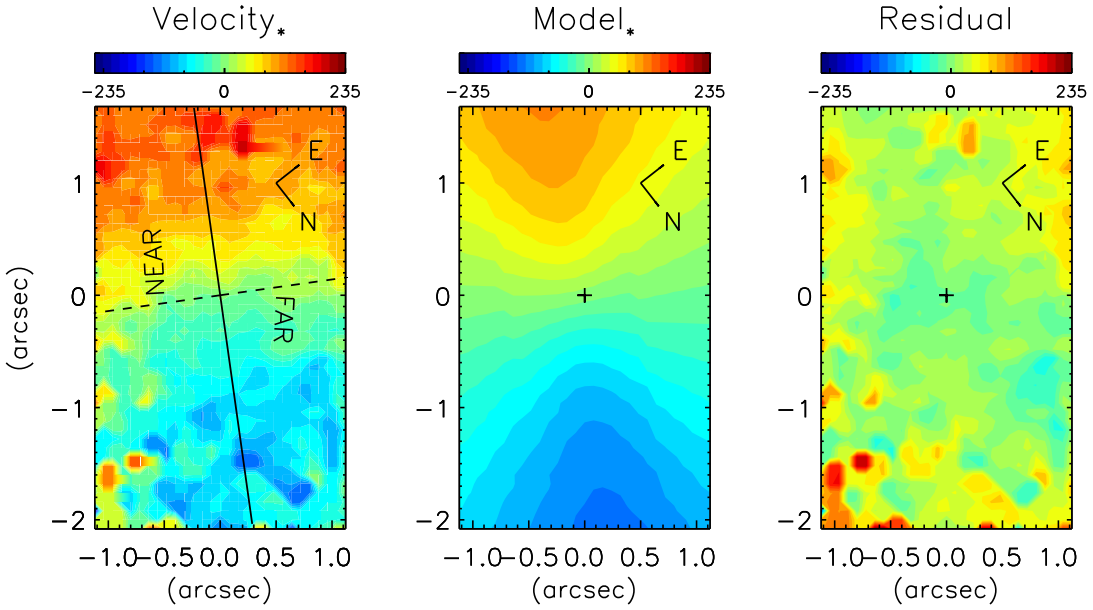

Figure 2. From left to right: the stellar radial velocity obtained with PPXF (spaxels were Voronoi-binned to get a minimal S/N of 25 in the continuum), the best-fitting Bertola rotation model, and the residual (PPXF velocity model) radial velocity field. Axes (in arcsec) are relative to the stellar continuum peak, indicated by the intersection of the solid and dashed lines (major and minor axis, respectively) in the radial velocity map and the black cross in the rotation model and the residual map. The panels follow the respective colour bars (units of km s^{-1}).

Table 1. Bertola model parameters: stars and H α.

Parameter	Value ($\star$)	Value (H α)
$\Delta V_{\rm sys}$	•45.16 km s^{-1}	*10 km s^{-1}
PA	150°	150°
i	48°	48°
A	•170 km s^{-1}	*500 km s^{-1}
c	•0.8	*1
p	•0.9	*1.9

Note. Rotation model parameters for stars and gas. Column 1: parameter name; Column 2: parameter value in best-fitting Bertola model to the stellar radial velocity field. Column 3: Same as Column 2 but for the H α radial velocity field. Values marked with an asterisk were determined by fits (by eye) to the PV diagrams (see the text). Values marked with a filled circle were determined using the Levenberg–Marquardt least-squares algorithm with an error of 10%.

The stellar radial velocity field obtained by PPXF is shown in the left-hand panel of Fig. 2: velocities range from −124 to 117 km s^{-1}, assuming a systemic velocity ($V_{\rm sys}$) 6790 ± 13 km s^{-1} (z = 0.022 6 ± 0.000 04), which is the average nuclear stellar radial velocity computed by PPXF . This map does not cover the complete GMOS/IFU FOV since fibres on the left and right edges (0.″5) have a very low S/N and thus could not be fitted with PPXF . The continuum peak is at the intersection of the solid and dashed black line. We modelled the stellar velocity field assuming circular orbits in a disc and a spherical potential following equation (2) of Bertola et al. (1991). This model has six parameters: an amplitude scaling of the velocity curve (A), the radius at which the maximum velocity is achieved (c), the behaviour of the velocity curve beyond its maximum value (e.g. flat or decreasing; p), the inclination of the disc (i), major axis PA (PA), and the systemic velocity. We fixed the major axis PA (150° following Schmitt & Kinney 2000) and the inclination (48°) and used the Levenberg–Marquardt least-squares algorithm within INTERACTIVE DATA LANGUAGE (IDL) to obtain the remaining four parameters of the Bertola model which best fit the observed stellar radial velocity field. The resulting parameters of the best-fitting model are listed in Table 1, and the best-fitting stellar velocity model and its residuals (PPXF radial velocity field model) are shown in the second and third panels of Fig. 2, respectively. While the observed radial velocity field is noisy, it appears that the model provides a reasonable fit to the data and supports a rotating stellar disc.

3.2 Single Gaussian emission line fitting

We used the IDL code PROFIT (Riffel 2010), which fits a single Gaussian to a given emission line, to derive the fluxes, radial velocities, and velocity dispersion, at each fibre, of the stronger emission lines (H β, [O III] λ5007 Å, H α, [N II] λλ6548,6584 Å and d [S II] λλ6717,6731 Å).

Fig. 3 presents the integrated flux (erg s^{-1} cm^{-2} fibre^{-1}), velocity field, and velocity dispersion of the [O III], H α and [N II] emission lines obtained from PROFIT. The zero velocity in the radial velocity maps corresponds to a systemic velocity of $V_{\rm sys}$ = 6790 km s^{-1}.

It is notable that while the flux of [O III] emission line peaks at the (continuum) nucleus, the H α and [N II] emission lines peak at a position 0.″25 to the NW along the major axis. The H α flux distribution is clearly asymmetric and extended to the NW in its brightest regions. The [N II] flux distribution (middle) is extended in an angle 20° from the major axis PA at all flux levels. As previously noted by Schmitt et al. (2003), the [O III] flux distribution is centred on the nucleus, and while it is more symmetrically distributed than the other two lines, it also shows a faint extension along the same PA as the [N II] line. The extension we see in [O III] is significantly larger than that reported by Schmitt et al. (2003) from *HST* imaging, presumably attributable to both the extra depth in our data and ground-based seeing.

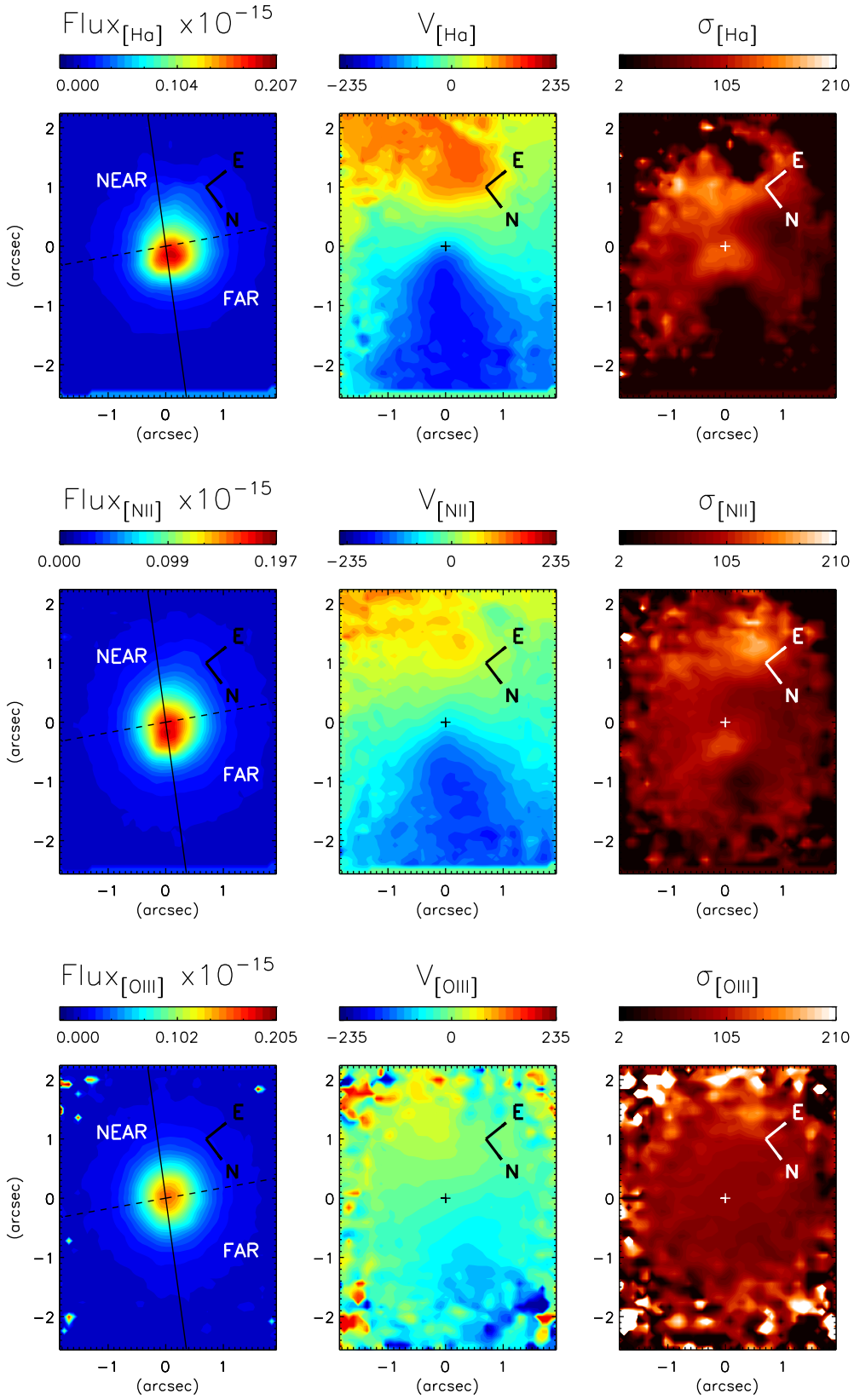

Figure 3. From left to right: maps of the flux (units of 10^{-15} erg s^{-1} cm^{-2} fibre^{-1} following the colour bar at the top of each panel), radial velocity (km s^{-1}), and velocity dispersion (km s^{-1}) derived from the single Gaussian fit to the H α (top row), [N II] λ6584 Å (middle row) and [O III] λ5007 Å (bottom row). Axes (in arcsec) are relative to the stellar continuum peak, indicated by the intersection of the solid and dashed lines in the flux maps and the white cross in the radial velocity and velocity dispersion maps. The solid (dashed) line indicates the major (minor) axis. The near (SW) and far (NE) sides of the disc are marked in the flux maps. Each panel follows the colour bar on top. The zero velocity corresponds to a systemic velocity of 6790 $\pm$ 13 km s^{-1}.

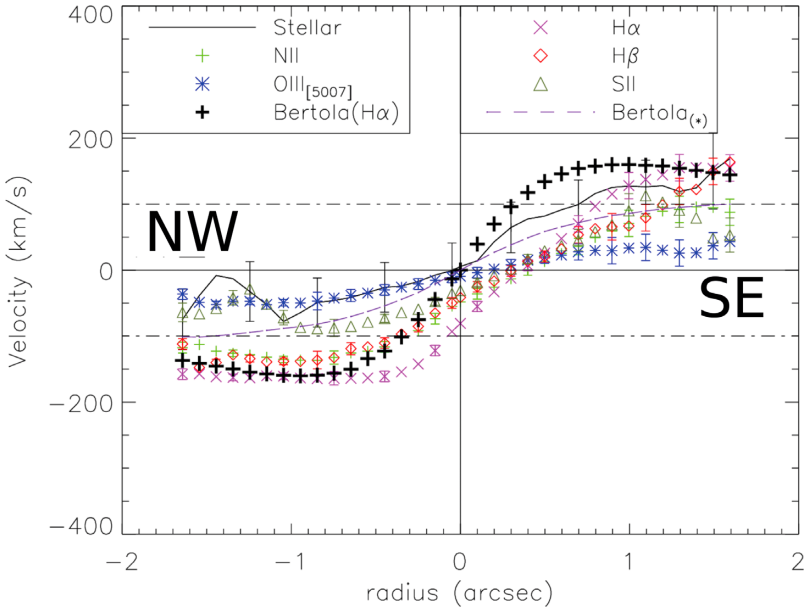

Figure 4. Observed and modelled rotation curves for emission lines and stars, assuming the nucleus to be cospatial with the stellar continuum peak and a systemic velocity of 6790 km s^{-1}. Symbols show the observed velocities from the single component Gaussian fit, extracted along the major axis (PA = 150°), for [S II] (dark green open triangles), [N II] (green plus signs), [O III] λ5007 Å (blue asterisks), H α (magenta crosses), and H β (red open diamonds). The stellar radial velocity field, as derived from PPXF and extracted along the same PA, is shown with the solid black line. Here, the velocities of the stellar Bertola model were offset by 45 km s^{-1} to pass through the central point at systemic velocity (see the text); error bars on the stellar velocities are as reported by PPXF. The predictions of the best-fitting Bertola rotation model for the stars and gas are shown with purple dashed lines and big black crosses, respectively (see the text).

The radial velocity maps for H α and [N II] (second column of Fig. 3) show a pattern broadly consistent with rotation in a disc with projected velocities up to ±180 km s^{-1}, but with notable distortions, especially to the south and east. While they are roughly similar, the H α emission line occasionally shows larger velocities when compared to the [N II] line. The [O III] radial velocity field, on the other hand, shows significantly lower projected velocities: close to systemic velocity in the inner 1 arcsec radius along the major axis and reaching only 60 km s^{-1} at larger radii.

The intrinsic velocity dispersion of the three emission lines, after deconvolution of the instrumental broadening (36 km s^{-1}), are shown in the right-hand panels of Fig. 3. The [O III] line shows a relatively uniform velocity dispersion map with values of ∼90 km s^{-1} in the inner 2 arcsec, and rising to 160 km s^{-1} in the outer regions (where the S/N ratio is lower). On the other hand, the H α and [N II] emission lines show variations in their dispersion. Both show relatively high (140 km s^{-1}) dispersion in the inner 0.″5 to the NW along the major axis, and H α also shows a high dispersion region along the major axis to the SE. The unusual redshifted region to the SE, noted above, shows a low dispersion in H α and a high (190 km s^{-1}) dispersion in [N II].

In Fig. 4, we present rotation curves of all the important emission lines, stellar component, and stellar and gas rotation models. These curves are the result of extracting the value of the velocities through the PA on each radial velocity map. We can observe that gaseous and stellar curves are not symmetric around the nucleus with higher values to the SE. We attribute this asymmetry to a systemic velocity component more clearly seen on the PV diagrams in Section 3.3.

Given the disagreements between the radial velocity fields of the prominent emission lines, and the asymmetries seen in individual emission line radial velocity fields, an obvious next step would be to attempt two component fits to the emission lines. However, our attempts at 'blind' two component fits failed in all cases since the second component is most likely close to systemic velocity and thus often indistinguishable (due to projection effects) from the rotating component except along the major axis of the galaxy. We thus first use PV diagrams and aperture spectra to best constrain the true gas rotation (next section), and then use this information to attempt tightly guided two-component fits to the emission lines in specific apertures.

3.3 Position–velocity diagrams

We made PV diagrams of all bright emission-lines along 18 PAs spaced by 10°, in order to better understand the multiple velocity components in the nuclear region of UGC 2024. Fig. 5 shows the most relevant of these PV diagrams for the H α+[N II]λ6584 Å and [O III] λ5007 Å lines: those along the major and minor axes, and four other other angles as indicated in each panel.

On each PV diagram we overplot the radial velocity obtained by the single Gaussian fit along the respective PA (white line); clearly these velocities are not representative of the rotating component of the H α and [N II] emission lines. In fact the velocities obtained by the single Gaussian fit typically lie between the clearly rotating component and the systemic velocity, a clear sign of a second lower velocity component.

Using a fixed PA (150°) and disc inclination ($i = 48°$) we adjusted the values of A, p, and c in order to obtain a Bertola rotation model which best (visually) fits the rotating component of H α along the galaxy major axis in the PV diagrams. The parameter values of this visual 'best-fitting' Bertola rotation model are listed in the third column of Table 1, and shown as the black solid line in all PV diagrams. This rotation model appears to fit the H α PV diagrams in all PAs, though in some (see below) PAs intermediate between the major and minor axes, the redshifted (SE) side of the galaxy –

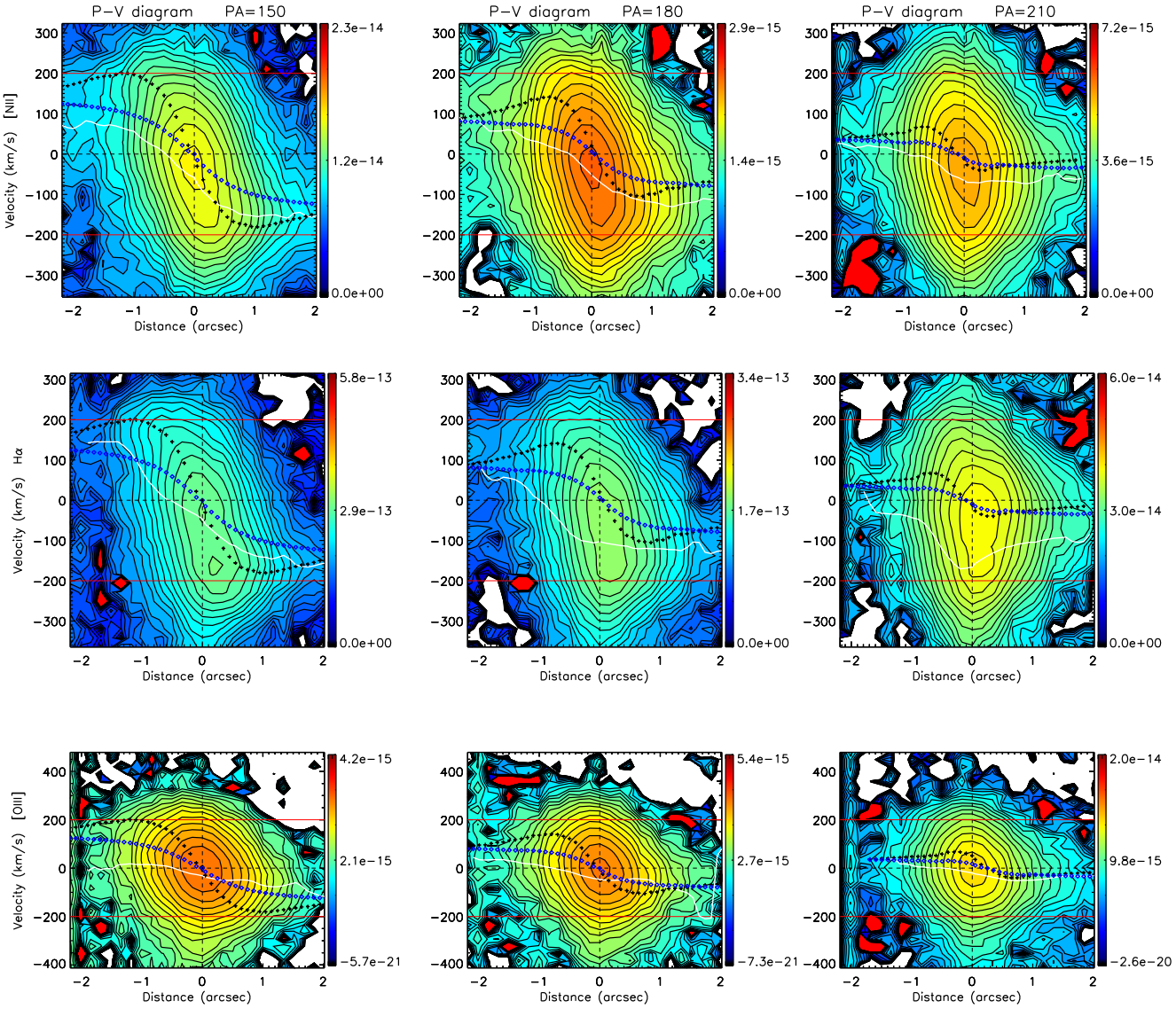

Figure 5. PV diagrams of the [N II] λ6584 Å (top), H α (middle) and [O III] λ5007 Å (bottom) emission lines. The angle in each column title is the PA on the sky (the major axis PA is 150°). The x-axis is the offset, in arcsec, from the stellar continuum peak, with the nuclear position delineated by the vertical dashed black line. The y-axis, in units of km s^{-1}, is relative to the adopted systemic velocity of 6790 km s^{-1}; the systemic velocity is delineated by the horizontal dashed black line. Horizontal solid red lines are drawn at −200 and 200 km s^{-1} as a guide to the eye. On each PV diagram we overplot the radial velocity predicted by the single Gaussian fit (solid white line), the prediction of the Bertola rotation model for the stars (blue diamonds) and the best (by eye, using all 18 PAs) Bertola rotation model for the gas (black plus signs).

specifically the unusual redshifted region to the SE of the nucleus earlier noted in Section 3.2 (see Fig. 6) – shows redshifted velocities larger than those predicted by the model. This H α Bertola model also provides a reasonable fit to the [N II] PV diagrams in all PAs. In both H α and [N II], the rotating component of the emission line gas is brighter than any secondary component of emission-line gas. The [O III] PV diagrams, however, are significantly different. Here, while there is evidence of faint emission consistent with the predictions of the H α Bertola model, this emission is not dominant; instead the bulk of the emission is found closer to systemic velocity (as compared to the rotation model in any given PA). We have also overplotted the Bertola rotation model of the stars in all PV diagrams for reference (solid white line); there does not appear to be any clear coincidence between this stellar rotation model and the gas velocities.

Having visually identified a best-fitting H α Bertola rotation model using the PV diagrams we now test this against the velocity field obtained by the single Gaussian fit. As discussed above the single Gaussian fit does not correctly track the rotation component of the H α and [N II] emission-lines. Nevertheless, the residual radial velocity field helps indicate the locations, and magnitudes, of additional velocity components which distort the single Gaussian fit.

The left-hand panel in Fig. 6 shows the best-fitting (by eye) H α Bertola rotation model, and the remaining panels of the same figure show the residual (subtracting this model from the radial velocity field obtained from the single Gaussian fit to the respective line) radial velocity fields of H α, [N II], and [O III]. The H α residual shows strong (up to −140 km s^{-1}) blueshifted residuals along the major axis to the SE and weaker redshifted residuals along the major axis to the NW. Additionally, the anomalous region to the SE

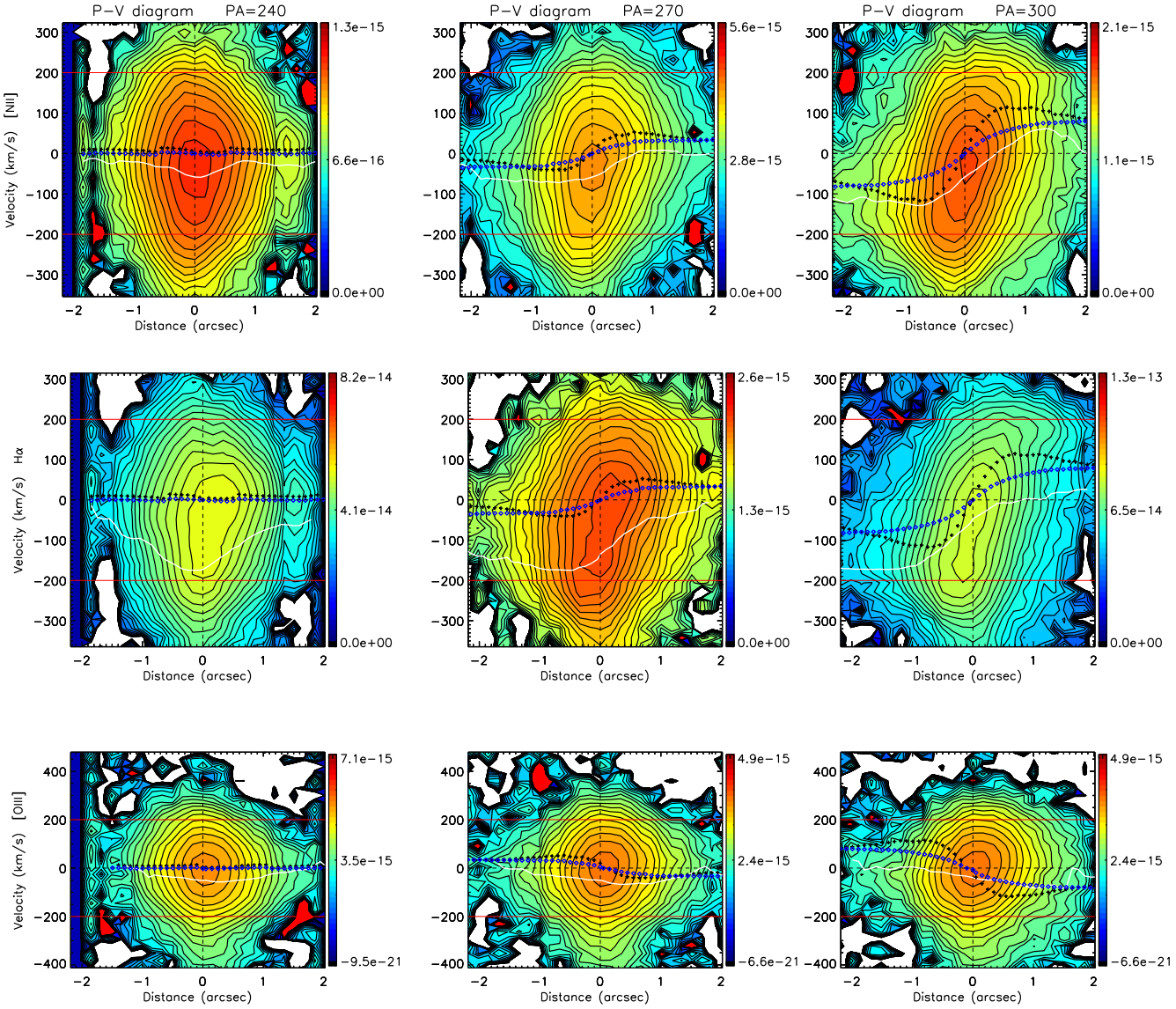

Figure 5. *–continued.*

shows intermediate (up to 25 km s^{-1}) redshifted residuals. The [N II] emission lines show stronger residuals (as compared to H α) along the major axis (44 km s^{-1} to the NE and −149 km s^{-1} to the SW), but smaller residuals in the SE anomalous region. The [O III] residual map is almost an inverse of the model velocity field, confirming that the brightest emission is centred on systemic velocity over most of the galaxy. Note also that the PA of the residual radial velocity in the [O III] residual radial velocity map is slightly tilted with respect to the PA of the galaxy major axis. Thus overall, the single Gaussian fit is always offset to velocities closer to systemic: the effect is weakest, but clearly present, in H α, intermediate in [N II], and strongest in [O III]. That is, we confirm the results seen in the PV diagrams, but now show that this is characteristic of the full radial velocity field rather than only in certain PAs.

3.4 Line profiles

To further visualize the asymmetric profiles of the emission lines, i.e. better constrain the second non-rotating component, Fig. 7 presents a continuum image of UGC 2024 for reference and the line profiles of the H α, [N II] and [O III] emission lines, extracted from seven different apertures (each of 0.″16 radius) in our GMOS data cube: a nuclear aperture, two apertures along the major axis, two apertures near the minor axis, one aperture in the anomalous (excessively redshifted) region to the SE of the nucleus, and one additional aperture. The three lines are overplotted after normalisation for easy comparison, and each panel indicates the x and y offset from the stellar continuum peak, the systemic velocity (dashed black line) and the expected rotation velocity in that aperture (solid brown line) as predicted by the best-fitting H α Bertola rotation model.

As pointed out earlier, the [O III] line (black spectrum) is predominantly centred on systemic velocity, with only slight shifts in its peak, or slight wings in its profile, towards the predicted rotation velocity of the respective aperture. Its full width at 10 per cent is 400 km s^{-1} in almost all apertures with high S/N ratio. Along the minor axis, the H α (double dot–dashed blue) and [N II] (dot–dashed red) lines, in profile and width, are similar to the [O III] line. Along the major axis, however, the H α line clearly shows two components,

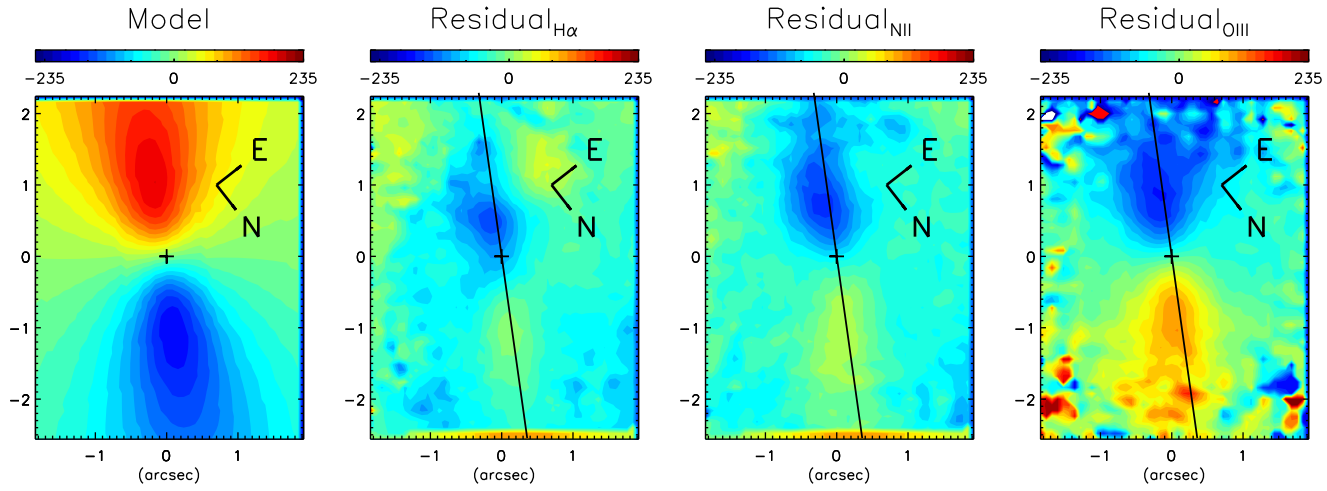

Figure 6. From left to right: the (visual) best-fitting H α Bertola rotation model (see the text), and the residual (single Gaussian fit radial velocity field – best-fitting H α Bertola model) radial velocity for H α, [N II], and [O III]. Each panel follows the colour bar (km s^{-1}) above it. The cross marks the stellar continuum peak in all panels, and the solid lines show the galaxy major axis PA.

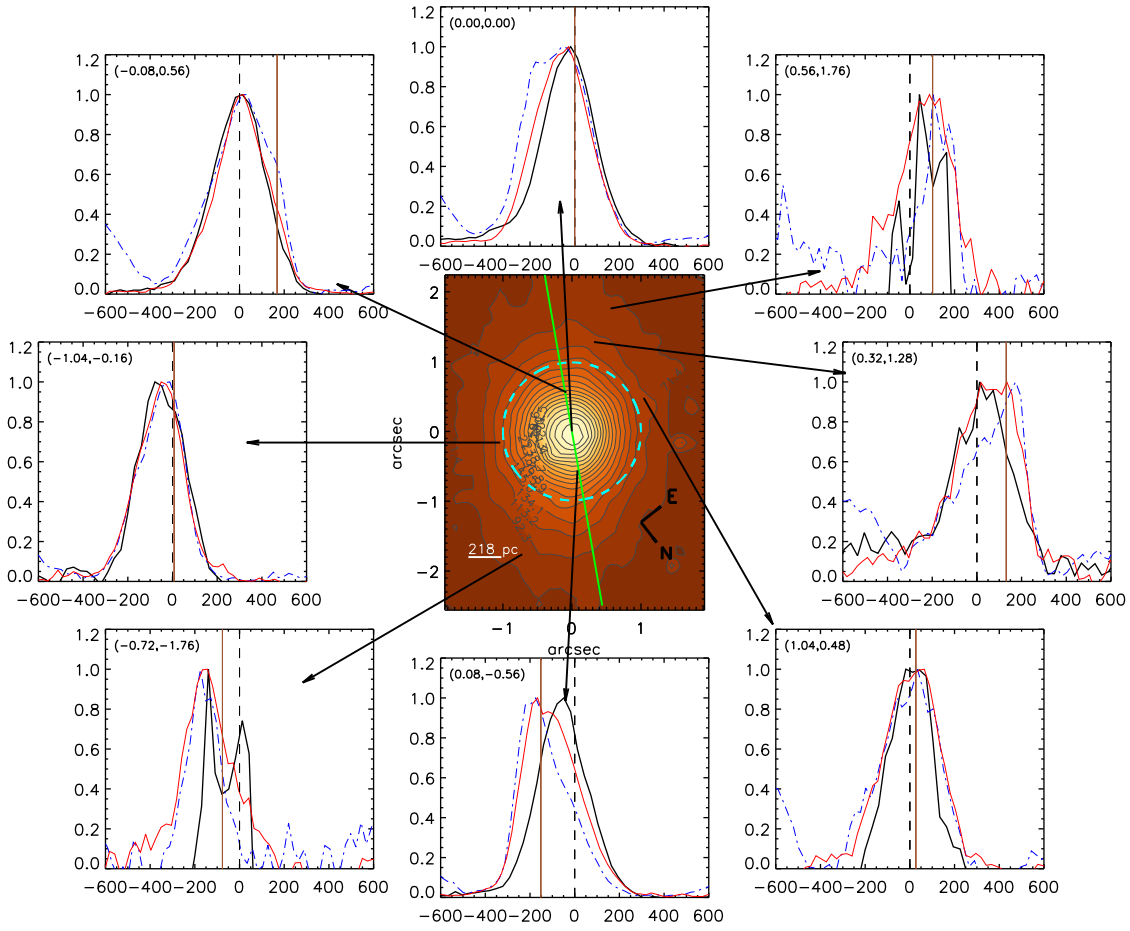

Figure 7. Line profiles of the [O III] (solid black), [N II] (triple dot–dashed red) and H α (dot–dashed blue) emission lines extracted from 0.″16 radius apertures centred on the offset positions (in arcsec) indicated in each panel. The offsets are calculated from the stellar continuum peak. The central panel shows the stellar continuum flux and contours, and the major axis as a solid green line: it is shown to illustrate the locations of the individual apertures. The dashed cyan circle is a guide to the eye to show the asymmetry of the light distribution. For easy comparison, the profiles are normalised and each panel indicates the systemic velocity (dashed black line) and the velocity expected from the best-fitting H α Bertola rotation model (solid brown line). The x-axis is in units of km s^{-1} centred on the systemic velocity.

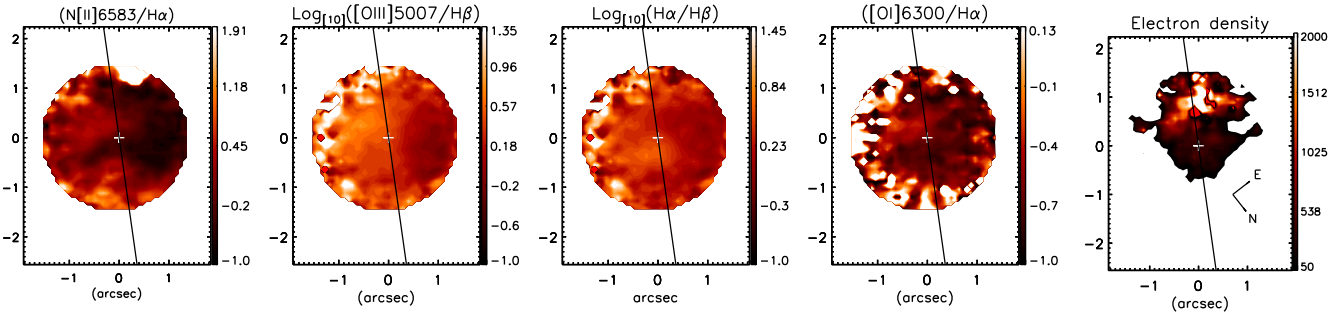

Figure 8. Emission line ratios (left to right: [N II]/H α, log([O III]/H β), log(H α/H β), and [O I]/H α) and the electron density (cm $^{-3}$) distribution, with each panel following the colourbar to its right. Note that the [O III]/H β and H α/H β ratios are shown in logarithmic scale. The white cross in each image indicates the stellar continuum peak and all panels have the same orientation, indicated by the compass in the rightmost panel. Axes scale are in arcseconds. Red points on the log([O III]/H β) and log(H α/H β) maps are pixels with low S/N in the H β emission line.

or one component with a clear wing: one close to the prediction of the rotation model and the other in agreement with the [O III] line (and thus systemic velocity). In general, when the two components are clearly separated, the rotating component shows stronger peak intensities, but is narrower, as compared to the systemic velocity component, but this dominance is not clear in every aperture. The [N II] line shows a behaviour intermediate between H α and [O III] and is clearly seen to well trace both the rotation component and systemic velocity component.

Velocity projection effects, and the coincidence between the width of the systemic velocity component and the maximum rotation velocities seen, means that we were unable to perform two component fits to the H α or [N II] line in all apertures. We thus chose four of the apertures shown in Fig. 7, where the two components are most clearly separated in velocity, and performed a double Gaussian fit (using our python codes) to the H α line. From these fits we found that, in median, 64 per cent of the profile area corresponds to the broad systemic velocity component ($\bar{\sigma}$ $\sim$135 km s^{-1}) and the remaining 36 per cent to the rotating component (narrow component with $\bar{\sigma}$ $\sim$69 km s^{-1}). We use this result in Section 4.1 to estimate the gas mass in the non-rotating component.

The top right panel of Fig. 7 shows the line profiles in the aperture extracted from the anomalously red region in the H α radial velocity map. This region presents very red velocities and low dispersion in the single Gaussian maps but the line profile shows that H α and [N II] have similar dispersion, driven primarily by the systemic velocity component. The single Gaussian fit failed to constrain the true dispersion here. This aperture coincides with the region where the S arm enters the nuclear region so the anomalous velocities observed here are likely a result of this large-scale anomalous spiral arm.

3.5 Gas excitation and electron density

We compute emission line ratios by dividing the flux maps obtained via the single Gaussian fits. Fig. 8 presents images of the [O III]/H β and H α/H β ratios on a log scale, plus the [N II]/H α and [O I]/H α line ratios, and the estimated electron density as derived from the [S II] λ6717/λ6731 line ratio, assuming a temperature of 10^4 K (Osterbrock & Ferland 2006). We show these line ratios only in the inner 3 arcsec region as within this region the emission lines (except [O I]) have S/N $>$ 20.

In general, all emission line ratios show higher values to the SW, i.e. the half of the disc which we earlier interpreted as the near side of the galaxy (Sect 3). Specifically the H α/H β ratio increases from 1.6 on the NE side of the nucleus to 7 on the SW side of the nucleus. Assuming that the intrinsic ratio is uniform in the disc, this implies a larger extinction on the SW side, supporting our interpretation that the near side of the disc is to the SW. The [N II]/H α ratio ranges from 0.8 ($-$0.1 dex) to 1.4 (0.1 dex) within the inner 1 arcsec radius with a value of 1 in the nucleus. The [O III]/H β ratio shows a similar behaviour, decreasing from SW to NE with values between 3.5 and 13.5 in the inner 1 arcsec radius and a value of 7.4 at the nucleus. These ratios, when plotted in BPT diagrams, are typical of Seyfert galaxies (e.g. James et al. 2005).

The electron density map is highly asymmetrical, with a peak value (1500 cm^{-3}) at a point 0.″3 SE from the nucleus and roughly along the major axis, a value of 730 cm^{-3} at the nucleus, and then decreasing to 200 cm^{-3} at 1 arcsec from the nucleus towards the NW. Considering that the correction of the telluric lines is not optimal, we estimate the errors on the electron density to be 30 per cent.

4 DISCUSSION

The continuum image in Fig. 7 shows that the stellar light distribution of the galaxy is more extended to the SW than to the NE in the inner 1 arcsec radius, highlighted by the dashed cyan circle, changing to a more homogeneous distribution at intermediate radii. Both the Gemini acquisition image and *HST* large-scale image in Fig. 1 show a prominent arm to the south and a fainter arm to the north with approximately the same extension of about 6 arcsec, beyond which they are both faint. These arms become less prominent as they move inwards to the nucleus but the *HST* large-scale image clearly shows that the S arm curves inwards and enters the brighter nuclear emission at about 1.″5 to the E. Both the PS nature of the galaxy (Goto 2006), and the possibility that this starburst phase could have been triggered by a previous interaction or minor merger, support the hypothesis of Heisler & Vader (1995) that the prominence of the spiral arm to the S could be due to the effects of a merger; however the presence of a twin fainter spiral arm to the N implies that the S arm is unlikely to be purely a stream of stars, or tidal tail, pulled out by the merger. Also, as the arm to the S is thicker and stronger than the one to the N, we propose that the (probably minor) merger occurred in the S of UGC 2024. The later is also supported by the anomalously redshifted (with respect to the expected rotation model) line profile seen in this area (e.g. the upper right panel in Fig. 7), and low dispersion in the H α single Gaussian radial velocity. This region seems to coincide with where the S arm enters the nuclear region, which could be the explanation of the larger velocities.

The presence of dust on the SW is not immediately obvious in the *HST* image, but the irregular contours present in the large-scale image, and the extension of the light distribution in the continuum and acquisition image support the presence of dust on this side. This confirms what we argue in Section 3.5, where we defined the near and far sides using the emission line ratios. Likewise, the large-scale image shows a little arm at 1.″5 eastwards. This arm changes its orientation beyond 1.″5 and smoothly connects with the southern thick arm, making it clear that the south arm is born in the E part of the galaxy. Comparing the position of the arms with the emission line radial velocity maps we can observe that one is placed in blue velocities and other in red ones. Together, these are signatures of trailing arms (Binney & Tremaine 2008).

Schmitt et al. (2003) argue that the [O III] distribution does not show a clear conical shape, even though such shapes are often seen in Seyfert 2 galaxies (Bae & Woo 2016). Anyway, from the PV diagrams in Section 3.3 we found a second component in this line, as well as in H α and [N II], with lower velocities than the ones observed by pure rotation in redshifted velocities (negative radii on the PV diagrams), showing that the single-Gaussian-fit velocities are being biased by a non-rotating component. By doing a double Gaussian fit to the H α line we verified the existence of a second velocity component with very low radial velocity values but with higher dispersion than the main rotational one. We also did double Gaussian fits to [O III], [N II], and H β in the same apertures we used for H α to estimate of the line ratios for the second component: $-0.187 < \log([\mathrm{N\,II}]/\mathrm{H}\alpha) < 0.115$ and $0.013 < \log([\mathrm{O\,III}]/\mathrm{H}\beta) < 0.67$. Studies by (Liu et al. 2013; Liu, Arav & Rupke 2015) in QSOs have shown that this high ionization plus the smooth velocity and high dispersion in [O III] are related to wide-angle cones or quasi-spherical outflows, so we are probably in the presence of an outflow with low radial velocity but high dispersion. The values of the emission line ratios show that the second component is also gas ionized by the AGN but near the region where the ionization could be caused by both star formation and AGN feedback on the BPT diagram (Baldwin, Phillips & Terlevich 1981).

Furthermore, we know that UGC 2024 is in a PS stage (Goto 2006) so the ionized gas which is not rotating could be either the named quasi-spherical outflow or ionized gas trapped in the halo after the starburst took place. This second scenario seems to be more suitable in the galaxy context since the PV diagrams revealed a very low radial velocity in the second component with values of 200 km s^{-1} (see Section 4.1), which means that the gas is unlikely to escape from the galaxy disc. We are unable to determine the time elapsed since the starburst ended as this requires knowledge of the fraction of the stellar mass produced in the burst and the burst duration (French et al. 2018). In any case, from the emission line ratios of the non-rotating component we can argue that the gas of this component have been 'recently cleaned' from the ionization caused by the starburst.

On the other hand, the H α and [N II] radial velocity fields present an 'S-shape' over our FOV and also the kinematic (rotation) centre is offset from the peak of the continuum. This shape is similar to the one found in NGC 3227 (Davies et al. 2014) and is commonly found in barred galaxies. (Storchi-Bergmann 2010; Schnorr-Müller et al. 2014b, 2016). In the EFIGI catalogue (Baillard et al. 2011), UGC 2024 is classified as a barred galaxy, but the effect of the bar is not strong enough to be clearly identified in our single or double Gaussian fits. Instead, we only note the effect in the variation of the kinematic centre of the radial velocity maps: this kinematic centre is offset 0.″3 (to the SE along the major axis) from the continuum peak. The complexities of separating the systemic velocity component from the rotating one are sufficiently high that, while there is likely an S-shaped structure in the radial velocity field, we are unable to quantitatively test for bar related perturbations in the rotating component of the velocity. However, since the perturbations in the rotating component appear to be one-sided instead of symmetric we posit that, the offset between continuum and continuum centres is more likely due to the anomalous arm rather than bar-related perturbations.

4.1 Mass and momentum in the non-rotating component

In the previous sections, we found the need to invoke a second non-rotating component in the ionized gas, and our best, though approximate, estimate is that two-thirds of the H α luminosity comes from it. Further, we have determined that this non-rotating component is centred on zero velocity and has a full width at 10 per cent of approximately 400 km s^{-1}. We can use these parameters to estimate the total mass in this non-rotating component, that we identify with a possible outflow.

The gas mass can be estimated as:

$$M_{\mathrm{g}} = m_{\mathrm{p}} N_{\mathrm{e}} V f, \tag{1}$$

where m_{p} is the proton mass, N_{e} is the electron density, obtained by using the method presented in Osterbrock (1989), V is the volume of the region where the outflow is detected and f is the filling factor. We can estimate the filling factor from:

$$L_{\mathrm{H}\alpha} \sim N_{\mathrm{e}}^2 j_{\mathrm{H}\alpha}(T) V f, \tag{2}$$

where $j_{\mathrm{H}\alpha} = 3.534 \times 10^{-25}$ erg cm^{-3} s^{-1} at $T = 10\,000$ K (Osterbrock 1989) and $L_{\mathrm{H}\alpha}$ is the H α luminosity emitted within the volume V. Then if we substitute equation (2) into equation (1), the mass can be expressed as:

$$M_{\mathrm{g}} = \frac{m_{\mathrm{p}} L_{\mathrm{H}\alpha}}{N_{\mathrm{e}} j_{\mathrm{H}\alpha}(T)}. \tag{3}$$

Considering a luminosity distance of 90 Mpc and using the total flux of H α in our GMOS FOV, we obtain $L_{\mathrm{H}\alpha} = 1.71 \pm 0.51 \times 10^{41}$ erg s^{-1}. The mean electron density within a 1.″5 radius aperture around the nucleus is $N_{\mathrm{e}} = 1312 \pm 7$ cm^{-3}. Thus, the total ionized gas mass is $\mathrm{M_g} \sim 3.26 \pm 0.45 \times 10^5$ M$_\odot$. Now, from the double Gaussian fits we performed in selected apertures we concluded that two-thirds of the H α emission comes from the non-rotating component, i.e. a mass of $2.1 \pm 0.29 \times 10^5$ M$_\odot$ belongs to the non-rotating component. From the residual radial velocity field in Fig. 6, it appears that the non-rotating component dominates out to at least 1.″5 radius. This component has a full width at 10 per cent of approximately 400 km s^{-1}. Under the assumption that it comes from a quasi-isotropic spherical outflow, the outflow velocity is 200 km s^{-1}.

We estimate the dynamical time as the ratio of the radius of the region where the outflow is observed (1.″5 $\sim$ 654 pc) to the velocity of the outflow. This gives a $T_{\mathrm{d}} \approx 3.2 \times 10^6$ yr so the mass outflow rate $\dot{M}$ is $6.5 \pm 0.22 \times 10^{-2}$ M$_\odot$ yr^{-1}.

For comparison, the mass accretion rate, ($\dot{M}_{\mathrm{acc}}$), onto the SMBH can be estimated from the AGN bolometric luminosity:

$$\dot{M}_{\mathrm{acc}} = \frac{L_{\mathrm{bol}}}{\eta c}, \tag{4}$$

where L_{bol} is the bolometric luminosity, η is the mass-to-energy conversion efficiency, assumed as 0.1 (Shakura & Sunyaev 1973) and c is the speed of light. We estimate L_{bol} using the relation

between [O III] and bolometric luminosity for low-luminosity galaxies using $L_{\rm bol} = 90 \times L_{\rm [O\,III]}$ (see Dumas et al. 2007). The total [O III] luminosity in our GMOS FOV is calculated to be $L_{\rm [O\,III]} = 2.37 \pm 0.7 \times 10^{41}$ erg s^{-1} and thus $L_{\rm bol} \approx 2.13 \pm 0.64 \times 10^{43}$ erg s^{-1}. Placing this value in equation (4) yields a mass accretion rate estimate of $\dot{M}_{\rm acc} \approx 3.8 \pm 0.5 \times 10^{-3}$ M$_\odot$ yr^{-1}. Thus the mass outflow rate, measured in the inner 1.″5 (654 pc) radius, is 17 times of the putative mass accretion rate onto the black hole, consistent with what was typically found in other AGNs (e.g. Riffel & Storchi-Bergmann 2011; Schnorr-Müller et al. 2014a; Lena et al. 2015) and indicates that the most of the outflowing gas originates in the larger scale nuclear interstellar medium, rather than very close to the AGN.

We estimated the escape velocity from the region where the non-rotating component is observable by using Veilleux et al. (2005) and obtained a value of $V_{\rm esc} = 350$ km s^{-1}. This is similar to the dispersion width of the second velocity component, and significantly higher than the estimated outflow velocity if the second component comes from an isotropic outflow. Thus, the second component is more likely a dispersion supported halo or a nuclear outflow 'fountain' which will not escape the galaxy. This ionized gas halo or fountain is likely a product of the recently concluded starburst phase of UGC 2024 which is currently being powered by the AGN.

5 CONCLUSIONS

We have observed the inner 3.″5 × 5″ of the Seyfert 2 galaxy UGC 2024 using the Gemini GMOS integral field unit over the wavelength range 4100–7300 Å, which includes important emission (H β, [O III] λλ4959,5007 Å, H α+[N II] λλ 6548,6584 Å, [S II] λλ6717,6731 Å) and absorption lines. We fitted the profiles of these lines and generated flux, radial velocity and velocity dispersion maps at a spatial resolution of 218 pc and a spectral resolution of 36 km s^{-1}. The complex kinematics, and the coincidence between the rotation component amplitude and the dispersion of a second component meant that our analysis done with PV diagrams and aperture spectra are more reliable than that from multiple component fits.

Our main conclusions are as follows:

(i) Dust structures, the assumption of trailing spiral arms and H α/H β ratios across the disc, all support the SW side as the near side of the galaxy disc.

(ii) The stellar continuum is asymmetric relative to the nucleus: it is brighter to the SW in the inner 1.″5 radius. While the [O III] emission is centred on the nucleus and symmetrically distributed, the H α and [N II] emission-lines peak about 0.″2 to the NW along the galaxy major axis and their distributions are asymmetric.

(iii) The [O III] radial velocity field is quasi-uniform and is centred close to the systemic velocity of the galaxy over the full FOV. The H α and [N II] emission lines, on the other hand, trace both this systemic velocity component and a component of gas rotating in the galaxy disc.

(iv) The rotation curves of strong emission lines, derived using single Gaussian fits, are asymmetric around the nucleus (Fig. 4), in part due to the posited systemic velocity component. The velocities of all strong emission lines are most in agreement at a point 0.″2 to the SW along the major axis, where all velocities are close to our chosen systemic velocity. This could point to offset kinematics produced by effects related to the bar perturbations, but less likely than the anomalous spiral arm or the fact that the flux of the non-rotating component is relatively weak here (e.g. Fig. 3) as compared to the equivalent point on the other side of the nucleus.

(v) Using PV diagrams and line profiles in several apertures, we were able to trace two kinematic components – one rotating and the other not – in the H α and [N II] emission lines, and fit a rotation model to the former component. Double Gaussian fits to the line profiles were used to constrain the widths of the two components. We found that the rotating component is narrow ($\bar{\sigma} \sim 69$ km s^{-1}) and the non-rotating component (centred near systemic velocity) is broader ($\bar{\sigma} \sim 135$ km s^{-1}).

(vi) The *HST* large-scale image shows that the two spiral arms in the galaxy are not symmetric. The S arm is prominent, while the N arm is faint. The former could be due to to the effects of a merger but the presence of the second one implies that the S arm is unlikely to be purely a stream of stars, or tidal tail, pulled out by the merger. The region where the anomalously bright S arm enters the nuclear region shows redshifts larger than those expected from pure rotation in the disc. This supports previous interpretations that the anomalous spiral arm is, at least in part, a product of a past minor merger. Also we posit that this anomalous arm is responsible for the offset between the stellar continuum peak and the emission line kinematic centre.

(vii) The coincidence between the width of the non-rotating velocity component and the maximum rotation velocities, means that we were unable to perform two component fits to the H α or [N II] line over the full FOV. Thus, we performed double Gaussian fits to four apertures where the two components were most easily distinguishable. We find that, on average, the rotating component accounts of one-third ($1.1 \pm 0.2 \times 10^5$ M$_\odot$) of the total ionized gas mass in the GMOS FOV ($M_{\rm g} \sim 3.3 \pm 0.5 \times 10^5$ M$_\odot$), while the systemic velocity component accounts for the remaining two-thirds of the mass.

(viii) The escape velocity in the region where the systemic velocity component is seen is 350 km s^{-1}, similar to the dispersion width of the non-rotating component, and higher than the estimated outflow velocity if this comes from an isotropic outflow. Thus, the systemic velocity component is more likely a dispersion supported halo or a nuclear outflow 'fountain' which will not escape the galaxy. This ionized gas halo or fountain is likely a product of the recently concluded starburst phase of UGC 2024 which is currently being powered by the AGN.

Given the complexity of the kinematics, with a non-rotating component detected over the full FOV of our observations, and kinematic disturbances related to the S anomalous spiral arm, future larger FOV (encompassing the full galaxy) and higher S/N ratio observations are necessary to better understand the role of outflows and other perturbations in UGC 2024.

ACKNOWLEDGEMENTS

This work is based on observations obtained at the Gemini Observatory, which is operated by the Association of Universities for Research in Astronomy, Inc., under a cooperative agreement with the NSF on behalf of the Gemini partnership: the National Science Foundation (United States), National Research Council (Canada), Comisión Nacional de Investigación Científica y Tecnológica (Chile), Ministerio de Ciencia, Tecnología e Innovación Productiva (Argentina), Ministério da Ciência, Tecnologia e Inovação (Brazil) and the Korea Astronomy and Space Science Institute (Republic of Korea). DM acknowledges support from CONICYT-PFCHA/Doctorado Nacional/2019-21191543. NN gratefully acknowledges support from CONICYT project BASAL AFB-170002

and PIA ACT172033. DM, NN, PH and PS acknowledges support from Fondecyt 1171506. VR was supported by the ALMA-CONICYT project 31140007 and BASAL AFB-170002. VF acknowledges support from CONICYT Astronomy Program-2015 Research Fellow GEMINI-CONICYT (32RF0002). RAR acknowledges support from FAPERGS and CNPq. This research has made use of the NASA/IPAC Extragalactic Database (NED) which is operated by the Jet Propulsion Laboratory, California Institute of Technology, under contract with the National Aeronautics and Space Administration.

REFERENCES

Allington-Smith J. et al., 2002, PASP, 114, 892
Bae H.-J., Woo J.-H., 2016, ApJ, 828, 97
Baillard A. et al., 2011, A&A, 532, A74
Baldwin J. A., Phillips M. M., Terlevich R., 1981, PASP, 93, 5
Barbosa F. K. B., Storchi-Bergmann T., McGregor P., Vale T. B., Rogemar Riffel A., 2014, MNRAS, 445, 2353
Bergmann T. S., 2012, in Chartas G., Hamann F., Leighly K. M., eds, ASP Conf. Ser. Vol. 460, AGN Winds in Charleston. Astron. Soc. Pac., San Fracisco, p. 133
Bertola F., Bettoni D., Danziger J., Sadler E., Sparke L., de Zeeuw T., 1991, ApJ, 373, 369
Binney J., Tremaine S., 2008, Galactic Dynamics, 2nd edn. Princeton Univ. Press, Princeton, NJ
Cappellari M., 2017, MNRAS, 466, 798
Cappellari M., Copin Y., 2003, MNRAS, 342, 345
Cappellari M., Emsellem E., 2004, PASP, 116, 138
Crenshaw D. M., Kraemer S. B., 2000a, ApJ, 532, 247
Crenshaw D. M., Kraemer S. B., 2000b, ApJ, 532, L101
Crenshaw D. M., Kraemer S. B., 2012, ApJ, 753, 75
Crenshaw D. M., Kraemer S. B., George I. M., 2003, ARA&A, 41, 117
Crook A. C., Huchra J. P., Martimbeau N., Masters K. L., Jarrett T., Macri L. M., 2007, ApJ, 655, 790
Davies R. D., 1972, in Evans D. S., Wills D., Wills B. J., eds, Proc. IAU Symp. 44, External Galaxies and Quasi-Stellar Objects. Dordrecht, Reidel, p. 67
Davies R. I. et al., 2014, ApJ, 792, 101
Dumas G., Mundell C. G., Emsellem E., Nagar N. M., 2007, MNRAS, 379, 1249
Ellison S. L., Patton D. R., Nair P., Mendel J. T., Scudder J. M., Simard L., 2013, in Sun W.-H., Xu C. K., Scoville N. Z., Sanders D. B., eds, ASP Conf. Ser. Vol. 477, Galaxy Mergers in an Evolving Universe. Astron. Soc. Pac., San Francisco, p. 7
Emsellem E., Goudfrooij P., Ferruit P., 2003, MNRAS, 345, 1297
Emsellem E., Fathi K., Wozniak H., Ferruit P., Mundell C. G., Schinnerer E., 2006, MNRAS, 365, 367
Englmaier P., Shlosman I., 2004, ApJ, 617, L115
Falcón-Barroso J., Sánchez-Blázquez P., Vazdekis A., Ricciardelli E., Cardiel N., Cenarro A. J., Gorgas J., Peletier R. F., 2011, A&A, 532, A95
Finlez C., Nagar N. M., Storchi-Bergmann T., Schnorr-Müller A., Riffel R. A., Lena D., Mundell C. G., Elvis M. S., 2018, MNRAS, 479, 3892
Fischer T. C., Crenshaw D. M., Kraemer S. B., Schmitt H. R., Trippe M. L., 2010, AJ, 140, 577
Fischer T. C., Crenshaw D. M., Kraemer S. B., Schmitt H. R., 2013, ApJS, 209, 1
French K. D., Yang Y., Zabludoff A. I., Tremonti C. A., 2018, ApJ, 862, 2
Gelbord J. M., Mullaney J. R., Ward M. J., 2009, MNRAS, 397, 172
Giuricin G., Mezzetti M., Mardirossian F., 1985, A&AS, 62, 157
Goto T., 2006, MNRAS, 369, 1765
Heisler C. A., De Robertis M. M., 1999, AJ, 118, 2038
Heisler C. A., Vader J. P., 1994, AJ, 107, 35
Heisler C. A., Vader J. P., 1995, AJ, 110, 87
Hook I. M., Jørgensen I., Allington-Smith J. R., Davies R. L., Metcalfe N., Murowinski R. G., Crampton D., 2004, PASP, 116, 425
Huchra J. P., Vogeley M. S., Geller M. J., 1999, ApJS, 121, 287
Humire P. K. et al., 2018, A&A, 614, A94
James P. A., Shane N. S., Knapen J. H., Etherton J., Percival S. M., 2005, A&A, 429, 851
Kinney A. L., Schmitt H. R., Clarke C. J., Pringle J. E., Ulvestad J. S., Antonucci R. R. J., 2000, ApJ, 537, 152
Knapen J. H., 2005, Ap&SS, 295, 85
Lena D. et al., 2015, ApJ, 806, 84
Lena D., 2014, eprint (arXiv:1409.8264)
Liu G., Zakamska N. L., Greene J. E., Nesvadba N. P. H., Liu X., 2013, MNRAS, 436, 2576
Liu G., Arav N., Rupke D. S. N., 2015, ApJS, 221, 9
Lynden-Bell D., 1969, Nature, 223, 690
Nair P. B., Abraham R. G., 2010, ApJS, 186, 427
Osterbrock D. E., 1989, Astrophysics of Gaseous Nebulae and Active Galactic Nuclei. University Science Books, Mill Valley, CA, p. 422
Osterbrock D. E., Ferland G. J., 2006, Astrophysics of Gaseous Nebulae and Active Galactic Nuclei. University Science Books, Sausalito, CA
Paturel G., Petit C., Prugniel P., Theureau G., Rousseau J., Brouty M., Dubois P., Cambrésy L., 2003, A&A, 412, 45
Pawlik M. M. et al., 2018, MNRAS, 477, 1708
Revalski M., Crenshaw D. M., Kraemer S. B., Fischer T. C., Schmitt H. R., Machuca C., 2018, ApJ, 856, 46
Riffel R. A., 2010, Ap&SS, 327, 239
Riffel R. A., 2013, Bol. Asoc. Argentina Astron. La Plata Argentina, 56, 13
Riffel R. A., Storchi-Bergmann T., 2011, MNRAS, 411, 469
Sánchez-Blázquez P. et al., 2006, MNRAS, 371, 703
Schmitt H. R., Kinney A. L., 2000, ApJS, 128, 479
Schmitt H. R., Ulvestad J. S., Antonucci R. R. J., Kinney A. L., 2001, ApJS, 132, 199
Schmitt H. R., Donley J. L., Antonucci R. R. J., Hutchings J. B., Kinney A. L., Pringle J. E., 2003, ApJ, 597, 768
Schnorr-Müller A., Storchi-Bergmann T., Nagar N. M., Robinson A., Lena D., Riffel R. A., Couto G. S., 2014a, MNRAS, 437, 1708
Schnorr-Müller A., Storchi-Bergmann T., Nagar N. M., Ferrari F., 2014b, MNRAS, 438, 3322
Schnorr-Müller A., Storchi-Bergmann T., Robinson A., Lena D., Nagar N. M., 2016, MNRAS, 457, 972
Schnorr-Müller A., Storchi-Bergmann T., Ferrari F., Nagar N. M., 2017a, MNRAS, 466, 4370
Schnorr-Müller A., Storchi-Bergmann T., Nagar N. M., Robinson A., Lena D., 2017b, MNRAS, 471, 3888
Sell P. H. et al., 2014, MNRAS, 441, 3417
Shakura N. I., Sunyaev R. A., 1973, A&A, 24, 337
Shlosman I., Begelman M. C., Frank J., 1990, Nature, 345, 679
Slater R. et al., 2018, A&A, 621, 23
Soltan A., 1982, MNRAS, 200, 115
Storchi-Bergmann T., 2010, in Peterson B. M., Somerville R. S., Storchi-Bergmann T., eds, Proc. IAU Symp. 267, Co-Evolution of Central Black Holes and Galaxies. Rio de Janeiro, Brazil, p. 290
Toba Y. et al., 2013, PASJ, 65, 113
Veilleux S., Shopbell P. L., Miller S. T., 2001, AJ, 121, 198
Veilleux S., Cecil G., Bland-Hawthorn J., 2005, ARA&A, 43, 769
Wild V., Kauffmann G., Heckman T., Charlot S., Lemson G., Brinchmann J., Reichard T., Pasquali A., 2007, MNRAS, 381, 543

This paper has been typeset from a TEX/LATEX file prepared by the author.